

## Plastic collapse of tapered, tip-loaded cantilevered beams

James F. Wilson<sup>†</sup>

*Department of Civil and Environmental Engineering, Duke University,  
Durham, North Carolina, 27708-0287, U.S.A.*

Nayer A. El-Esnawy<sup>‡</sup>

*Department of Civil Engineering, Cairo University, Cairo, Egypt*

**Abstract.** The plastic collapse loads and their locations are predicted for a class of tapered, initially curved, and transversely corrugated cantilevered beams subjected to static tip loading. Results of both closed form and finite element solutions for several rigid perfectly plastic and elastic perfectly plastic beam models are evaluated. The governing equations are cast in nondimensional form for efficient studies of collapse load as it varies with beam geometry and the angle of the tip load. Static experiments for laboratory-scale configurations whose taper flared toward the tip, complemented the theory in that collapse occurred at points about 40% of the beams length from the fixed end. Experiments for low speed impact loading of these configurations showed that collapse occurred further from the fixed end, between the 61% and 71% points. The results may be applied to the design of safer highway guardrail terminal systems that collapse by design under vehicle impact.

**Key words:** beam dynamics; elastic buckling; cantilevered beam; corrugated cross section; curved beam; guardrail; impact loading; initial curvature; plastic collapse; plastic hinge; tapered beam.

### 1. Introduction

Tapered structural members such as beams and columns are employed in a wide variety of engineering applications. Examples in the open literature that involved elastic buckling of axially loaded beams with several types of cross sections, end fixities, and tapered profiles were reported by Dinnik (1932), Timoshenko and Gere (1961), Ermopoulos (1986), Williams and Aston (1989), and Siginer (1992). Problems in static and dynamic stability of linear elastic plane structures consisting of end-loaded, tapered beams were presented by Karabalis and Besko (1982), who also included a comprehensive survey of the related literature. In a companion paper to the present investigation, Wilson and Strong (1997) predicted elastic buckling loads for tip-loaded, tapered, cantilevered beams with thin-walled corrugated sections and initial beam curvature. The present investigation is an extension of the latter study in that plastic collapse of such configurations is analyzed and impact experiments are included. Expanded discussions of the static analyses presented herein were given by El-Esnawy (1997).

---

<sup>†</sup> Professor

<sup>‡</sup> Assistant Professor

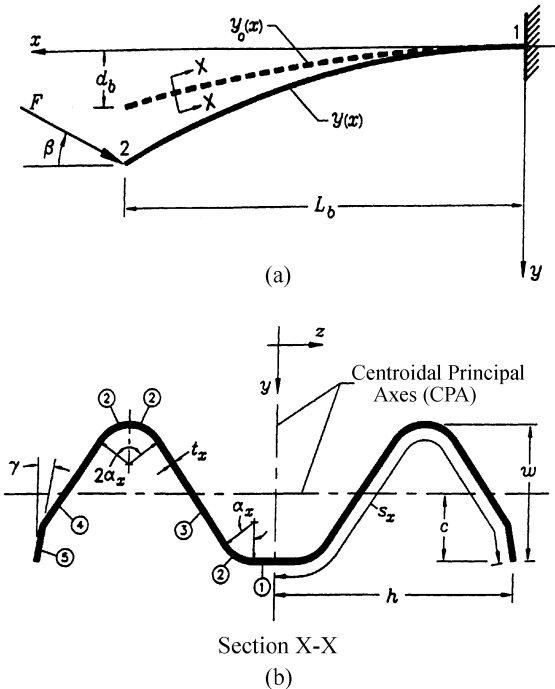


Fig. 1 Model of the initially curved, cantilevered beam: (a) geometric characteristics and tip load in the  $xy$ -plane; (b) typical full W-section in the  $yz$ -plane

The results herein are readily applicable to new designs of cantilevered guardrail terminal structures for our nation's highways, structures that, when impacted at the tip by an errant vehicle, would undergo plastic collapse without spearing (penetrating) the vehicle, Pigman and Agent (1988). In such a structure, modeled in Fig. 1, the flare of the tapered profile broadens from the fixed end to the tip so that plastic collapse would occur along its length rather than at the fixed end, as it would for a uniform section. The location of the gross plastic collapse mode depends on the configuration's material, initial curvature, taper profile, and tip loading rate (static or low velocity impact), and all of these factors are addressed in the present study.

Compared are the collapse loads and their locations based on several types of analysis: the plastic hinge technique (Horne 1979), a computer-aided frame analysis (Lee and Goel 1986), and finite element modeling (Maker *et al.* 1991). These analyses involved either a rigid-perfectly plastic material, or an elastic-perfectly plastic material, where geometric nonlinearities were sometimes included. We begin by modeling a general class of cantilevered beams, proceed by formulating several theories for plastic collapse, and conclude by applying the theories to predict the plastic collapse loads and their locations as functions of nondimensional system parameters. We then illustrate the theories with numerical studies of several terminal structures, and conclude this study with complementary experimental results for both static and impact loading.

## 2. Beam characteristics

The cantilevered beam structure is defined in Figs. 1 in which  $x$  is the longitudinal axis whose

origin is the centroid of the beam section located at the fixed end. The beam length is  $L_b$  and the end load  $F$  is inclined at angle  $\beta$  to the  $x$ -axis. The unloaded beam has the initially curved configuration  $y_o(x)$  of the form

$$y_o(x) = d_b \left( \frac{x}{L_b} \right)^2 \quad (1)$$

where  $d_b$  is its initial transverse end displacement relative to the fixed end. The beam has a corrugated cross section (W-section) whose general dimensions are defined in Fig. 1(b). This W-section has one plane of symmetry through the transverse  $y$ -axis where the  $y$ -axis is the centroidal principal symmetry-axis of the W-section. It comprises straight segments (denoted by 1, 3, 4, and 5) and circular segments (denoted by 2), where the straight segments are tangent to the adjacent circular segments. At location  $x$ , the section properties are fully defined by the thickness  $t_x$ , the arc length  $s_x$ , and the angle  $\alpha_x$ . These properties are

$$w(x) = s_x G_1(\alpha_x) \quad (2a)$$

$$A(x) = 2s_x t_x \quad (2b)$$

$$c(x) = s_x G_2(\alpha_x) \quad (2c)$$

$$I(x) = \frac{1}{12} s_x^3 t_x G_3(\alpha_x) + \frac{\eta_1}{6} s_x t_x^3 \quad (2d)$$

$$h(x) = \left( \eta_1 + \eta_5 (\eta_3 + \eta_4) \cos \alpha_x \cos \gamma(x) + 3 \eta_2 \frac{\sin \alpha_x}{\alpha_x} \right) s_x \quad (2e)$$

$$\gamma(x) = \arcsin \left( \frac{1}{2 \eta_5} [G_1(\alpha_x) + (\eta_3 - 2 \eta_4) \sin \alpha_x] \right) \quad (2f)$$

where  $w$  is the corrugation depth,  $A$  is the cross sectional area,  $c$  is the location of the centroidal principal asymmetry-axis which is parallel to the transverse  $z$ -axis,  $I$  is the second area moment about the centroidal principal asymmetry-axis,  $h$  is half the corrugation width, and  $\gamma$  is the angle of the straight segment or item 5. In Eqs. (2),  $G_j(\alpha_x)$ ,  $j=1,2,\dots,5$ , defined in the Appendix, are functions of the corrugation angle; and  $\eta_i$ ,  $i=1,2,\dots,5$ , are ratios of the length or arc length of the  $i$ th straight or circular segment to  $s_x$ .

The cantilevered beam is tapered along its length such that the ratios  $\eta_i$  are constant, and the thickness of the corrugation is constant ( $t_x=t$ ). Also, the arc length and the angle of the corrugation vary linearly with beam length, or

$$s_x = s_1 + \frac{(s_2 - s_1)}{L_b} x \quad (3)$$

$$\alpha_x = \alpha_1 + \frac{(\alpha_2 - \alpha_1)}{L_b} x \quad (4)$$

In Eqs. (3) and (4),  $s_1$  and  $\alpha_1$  are the arc length and the angle of the corrugation at the fixed end, respectively, where  $s_2$  and  $\alpha_2$  are those parameters at the free end. The variation of  $s_x$  reflects the form of the initially flat sheet used to form W-section. The linear variation of the arc length of the corrugation given by Eq. (4) indicates that this initially flat sheet is either a trapezoid ( $s_2 \neq s_1$ ) or a rectangle ( $s_2 = s_1$ ).

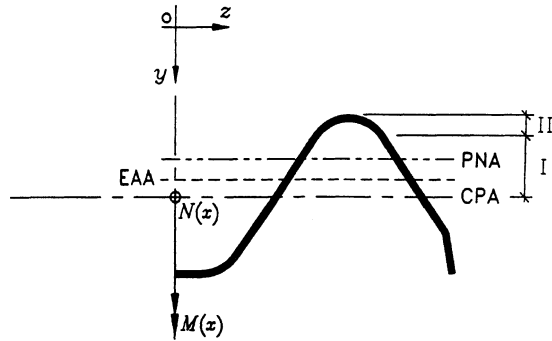


Fig. 2 Schematic of half W-section of the beam model showing the CPA, EAA, and PNA , and the directions of the normal compressive force and the bending moment due to tip load

### 3. Theory for plastic collapse

Consider now the case of bending of the W-section about the centroidal principal asymmetry-axis (CPA) as shown in Fig. 2. Assume that the beam is perfectly-plastic beyond its yield stress  $\sigma_y$  so that static plastic collapse may be computed using the plastic hinge technique in which this hinge occurs at a section with the fully plastic moment  $M_{FP}$ . A single plastic hinge is sufficient for the collapse of the cantilevered beam of Fig. 1. The fully plastic moment is reduced by both the normal compressive force  $N(x)$  and the transverse shear force due to the tip load. The effect of the transverse shear force may be neglected for shallow angles of the tip load, (Horne and Morris 1982). Thus, considering only the effect of  $N(x)$ , the reduced plastic moment  $M_{RP}$  of the W-section at a distance  $x$  along the beam length, determined about the CPA, is given by

$$M_{RP}(x) = M_{FP}(x) - k_1[f(\alpha_x, \lambda(x)) + k_2\lambda(x)(G_4(\alpha_x) - G_2(\alpha_x))]N_y(x)s_x \quad (5a)$$

in which

$$M_{FP}(x) = Z_{FP}(x)\sigma_y \quad (5b)$$

$$\lambda(x) = \frac{N(x)}{N_y(x)} \quad (5c)$$

In Eq. (5a), the term multiplying  $k_1$  represents the effect of the normal compressive force  $N(x)$ .  $k_1$  and  $k_2$  are indicators with values of 0 or 1.  $Z_{FP}$ , the plastic modulus of the W-section in the absence of the normal compressive force, is computed by taking the first moment of area about the equal area axis (EAA), the axis that divides the W-section into two equal areas, assigning a positive sign to the moment on either side of the EAA. That is

$$Z_{FP}(x) = 2ts_x^2G_5(\alpha_x) \quad (6)$$

Further, the term  $\lambda(x)$  defined by Eq. (5c) is referred to as the squash load ratio, where  $N_y(x)$  is the maximum normal load carrying capacity of the W-section for the case of no bending moment (the squash load), or

$$N_y(x) = A(x)\sigma_y = 2ts_x\sigma_y \quad (7)$$

The function  $f(\alpha_x, \lambda(x))$  in Eq. (5a) depends on the location of the plastic neutral axis (PNA), the neutral axis for a fully plastic W-section. In the absence of  $N(x)$ , the PNA and the EAA are coincident. In the presence of  $N(x)$ , the PNA moves in the negative  $y$ -direction (see Fig. 2). If the squash load ratio satisfies the inequality  $\lambda(x) \leq (1-4\eta_2)$ , then the PNA will lie across the straight segments denoted by 3 and 4 (Region I in Fig. 2); otherwise it will lie across the top circular segments denoted by 2 (Region II). For the former case,

$$f(\alpha_x, \lambda(x)) = \frac{1}{8}(\lambda(x))^2 \sin \alpha_x \quad (8)$$

For the latter case,

$$\begin{aligned} f(\alpha_x, \lambda(x)) &= \frac{1}{8}(1-4\eta_2)^2 \sin \alpha_x - \frac{4\eta_2^2}{\alpha_x^2} \left( \sin \left[ \frac{\alpha_x}{4\eta_2} (1-\lambda(x)) \right] - \sin \alpha_x \right) \\ &\quad - (1-4\eta_2 - \lambda(x)) \left( G_1(\alpha_x) - G_4(\alpha_x) - \frac{\eta_2}{\alpha_x} \right) \end{aligned} \quad (9)$$

The term multiplying  $k_2$  in Eq. (5a) represents the difference between the location of the EAA and the location of the CPA. If this difference is sufficiently small, then  $k_2=0$ ; if the effect of  $N(x)$  is also sufficiently small, then  $k_1=0$ ; otherwise  $k_1=k_2=1$ . At this point, with little loss in generality,  $k_2=0$  is assumed hereafter.

The tip load  $F$  lies in the plane of the centroidal axes of the W-section. Its inclination angles are assumed to lie in the range  $\beta=0$  to 15 degrees. For small elastic beam deformations, the changes of  $L_b$  and  $\beta$  during loading are also small, for which the normal compressive force and the bending moment at  $x$  become, respectively

$$N(x) = \left[ \cos \beta - \frac{dy(x)}{dx} \sin \beta \right] F \quad (10)$$

$$M(x) = [(L_b - x) \sin \beta + (y_2 - y(x)) \cos \beta] F \quad (11)$$

where  $y(x)$  and  $y_2$  are the elastic transverse displacement curve and tip displacement, respectively.

Neglect now the effect on beam deformations of the spread of the plastic zone from the time of the first yield to the time that the W-section becomes fully plastic. Then, the plastic hinge occurs at the W-section where the bending moment due to  $F$  given by Eq. (11) approaches the plastic moment given by Eq. (5a). The tip load at which the plastic hinge occurs is defined as the gross plastic collapse load,  $F_{GP}$ . Note that for a uniform cantilevered beam, the plastic hinge occurs at the fixed end; but for a tapered cantilevered beam, the plastic hinge can occur at any section along the beam length, and this location is especially sensitive to changes in  $\beta$ . Considering the effect of  $N(x)$ , the reduced plastic moment curve forms an envelope which is tangent to the bending moment curve corresponding to the gross plastic collapse load at the location of the plastic hinge  $x_p$ , or

$$M(x) = M_{RP}(x) \quad \text{at } x = x_p, \text{ and } F = F_{GP} \quad (12)$$

$$\frac{dM(x)}{dx} = \frac{dM_{RP}(x)}{dx} \quad \text{at } x = x_p, \text{ and } F = F_{GP} \quad (13)$$

In summary, Eqs. (12) and (13) can be used to compute the gross plastic collapse load,  $F_{GP}$ , and the location of the corresponding plastic hinge,  $x_p$ . However, if  $x_p$  so obtained lies outside its range

of  $0-L_b$ , then the feasible solution is that the plastic hinge occurs at the fixed end,  $x_p=0$ . In this case, only Eq. (12) governs the determination of  $F_{GP}$ .

#### 4. Special cases

Consider special cases in which the closed form solutions just discussed lead directly to the collapse loads and their locations. That is, apply Eqs. (12) and (13) for cases in which the PNA lies in Region I of Fig. 2, where the function  $f(\alpha_x, \lambda(x))$  in Eq. (5a) is given by Eq. (8). For example, for the W-section of a typical steel highway guardrail, the term  $(1-4\eta_2)\approx 0.6$ ,  $\sigma_y = 345 \text{ MN/m}^2$ , and the maximum normal load carrying capacity  $N_y(x)$  is about 0.46 MN. This load is equivalent to an impacting vehicle of mass 2200 kg having a constant deceleration of 21 g, where g is the acceleration due to gravity. Thus,  $\lambda(x) \leq 0.6$  where  $N(x) \leq 60\%$  of  $N_y(x)$ , is the practical range for a guardrail terminal's tip load. For this case, Eqs. (12) and (13) may be expressed in nondimensional form using the following notation: an over-bar for a nondimensional parameter, and a subscript  $p$  for a parameter evaluated at the location of the plastic hinge. In these terms, Eq. (12) becomes

$$\bar{s}_p^2 G_5(\alpha_p) - \frac{k_1}{8} \bar{F}_{GP}^2 \bar{N}_p^2 \sin \alpha_p - \bar{F}_{GP} \bar{l} [ (1 - \bar{x}_p) \sin \beta + (\bar{y}_2 - \bar{y}_p) \cos \beta ] = 0 \quad (14)$$

and Eq. (13) becomes

$$\begin{aligned} & \bar{s}_p^2 (\alpha_2 - \alpha_1) \frac{dG_5(\alpha_x)}{d\alpha_x} \Big|_{\alpha_x = \alpha_p} + 2\bar{s}_p (\bar{s}_2 - 1) G_5(\alpha_p) \\ & - \frac{k_1}{8} \bar{F}_{GP}^2 \bar{N}_p \left( \bar{N}_p (\alpha_2 - \alpha_1) \cos \alpha_p + 2 \frac{d^2 \bar{y}}{d\bar{x}^2} \Big|_{\bar{x} = \bar{x}_p} \sin \beta \sin \alpha_p \right) + \bar{F}_{GP} \bar{l} \left( \sin \beta + \frac{d\bar{y}}{d\bar{x}} \Big|_{\bar{x} = \bar{x}_p} \cos \beta \right) = 0 \end{aligned} \quad (15)$$

The nondimensional system parameters in the latter two equations are defined by

$$\bar{x} = \frac{x}{L_b}, \quad \bar{x}_p = \frac{x_p}{L_b} \quad (16)$$

$$\bar{y} = \frac{y(x)}{L_b}, \quad \bar{y}_p = \frac{y(x_p)}{L_b}, \quad \bar{y}_2 = \frac{y(L_b)}{L_b} \quad (17)$$

$$\bar{F}_{GP} = \frac{F_{GP}}{2ts_1\sigma_y}, \quad \bar{l} = \frac{L_b}{s_1} \quad (18)$$

$$\alpha_p = \alpha_1 + (\alpha_2 - \alpha_1) \bar{x}_p \quad (19)$$

$$\bar{s}_p = \frac{s_p}{s_1} = 1 + (\bar{s}_2 - 1) \bar{x}_p, \quad \bar{s}_2 = \frac{s_2}{s_1} \quad (20)$$

$$\bar{N}_p = \cos \beta - \frac{d\bar{y}}{d\bar{x}} \Big|_{\bar{x} = \bar{x}_p} \sin \beta \quad (21)$$

Eqs. (14) and (15) are nonlinear and a numerical scheme such as Newton-Raphson, together with *Mathematica* (Wolfram 1993) may be used to solve these equations simultaneous for  $\bar{F}_{GP}$  and  $\bar{x}_p$ .

If the effect of the normal compressive force in Eqs. (14) and (15) is neglected ( $k_1=0$ ), then an

upper bound on the gross plastic collapse load may be computed using Eq. (14), which becomes

$$\bar{F}_{GP}^u = \frac{\bar{s}_p^2 G_5(\alpha_p)}{l[(1-\bar{x}_p)\sin\beta + (\bar{y}_2 - \bar{y}_p)\cos\beta]} \quad (22)$$

Substituting Eq. (22) into Eq. (15) yields

$$\begin{aligned} & \bar{s}_p^2(\alpha_2 - \alpha_1) \frac{dG_5(\alpha_x)}{d\alpha_x} \Big|_{\alpha_x = \alpha_p} + 2\bar{s}_p(\bar{s}_2 - 1)G_5(\alpha_p) \\ & + \frac{\bar{s}_p^2 G_5(\alpha_p) \left( \sin\beta + \frac{d\bar{y}}{d\bar{x}} \Big|_{\bar{x} = \bar{x}_p} \cos\beta \right)}{[(1-\bar{x}_p)\sin\beta + (\bar{y}_2 - \bar{y}_p)\cos\beta]} = 0 \end{aligned} \quad (23)$$

Eq. (23) can be solved for  $\bar{x}_p$ , with which  $\bar{F}_{GP}^u$  is calculated from Eq. (22). Recall that if solving Eqs. (14) and (15), or solving Eq. (23) only, there results a value for  $\bar{x}_p$  outside its range of  $\bar{x}_p=0$  to 1, then the feasible solution is  $\bar{x}_p=0$ . In this case, the gross plastic collapse load or its upper bound is governed by Eq. (14) or Eq. (22), respectively.

It is observed that Eqs. (14) and (15) require the beam's elastic curve  $(\bar{y}, \bar{y}_p, \bar{y}_2)$ , which may be difficult to implement because of the change of the beam geometry during loading. However, this problem is overcome in the following two examples: one for a beam of a rigid perfectly plastic material, and the other for a beam with elastic perfectly plastic behavior.

For the first example, the rigid perfectly plastic beam, the beam's transverse displacement curve before yielding may be expressed in nondimensional form as

$$\bar{y} = \frac{y_o(x)}{L_b} = \Delta_b \bar{x}^2, \quad \Delta_b = \frac{d_b}{L_b} \quad (24)$$

For this example,  $\bar{y}_p = \Delta_b \bar{x}_p^2$  and  $\bar{y}_2 = \Delta_b$ , with the result that  $F_{GP}$  is always higher than the true static plastic collapse load of the beam.

For the second example, choose an approximate variation of  $I_a(x)$  in the form of a power law in  $x$ , as employed by Timoshenko and Gere (1961), Ermopoulos (1986), Wilson and Strong (1997), and Al-Gahtani (1996). That is

$$I_a(x) = I_1 \left[ 1 - (1 - \sqrt{\kappa}) \frac{x}{L_b} \right]^2 \quad (25)$$

where  $\kappa$  is the taper ratio defined by

$$\kappa = \frac{I_2}{I_1} \quad (26)$$

and  $I_1$  and  $I_2$  are the exact values of the second area moments of the W-section of the beam at the fixed end and the free end, respectively. From classical beam theory, it follows that the elastic curve  $y_{la}(x)$  obeys the following differential equation in which  $E$  is Young's modulus.

$$EI_a(x) \left[ \frac{d^2 y_{la}(x)}{dx^2} - \frac{d^2 y_o(x)}{dx^2} \right] = [(L_b - x)\sin\beta + (d_b - y_o(x))\cos\beta]F \quad (27)$$

In nondimensional form, using  $\bar{y}_{la} = y_{la}(x)/L_b$ , Eq. (27) becomes

$$\begin{aligned}\bar{y}_{la} &= \Delta_b \bar{x}^2 + \bar{F} \bar{Q} \left[ g_1(\kappa, \beta, \Delta_b) - \frac{\Delta_b \bar{x} \cos \beta}{2(1 - \sqrt{\kappa})^2} \right] \bar{x} + \bar{F} \bar{Q} \left[ \frac{g_1(\kappa, \beta, \Delta_b)}{1 - \sqrt{\kappa}} - g_2(\kappa, \beta, \Delta_b) \bar{x} \right] \\ &\quad \ln [1 - (1 - \sqrt{\kappa}) \bar{x}] \end{aligned}\quad (28)$$

$$\bar{F} = \frac{F}{2ts_1\sigma_y}, \quad \bar{Q} = \frac{\pi^2 ts_1 \sigma_y}{2Q_{cr}}, \quad Q_{cr} = \frac{\pi^2 EI_1}{4L_b^2} \quad (29)$$

$$g_1(\kappa, \beta, \Delta_b) = \frac{(1 - \kappa) \sin \beta + \Delta_b (2 - \kappa + 2\sqrt{\kappa}) \cos \beta}{(1 - \sqrt{\kappa})^3} \quad (30)$$

$$g_2(\kappa, \beta, \Delta_b) = \frac{(1 - \sqrt{\kappa}) \sin \beta + 2\Delta_b \cos \beta}{(1 - \sqrt{\kappa})^3} \quad (31)$$

In Eq. (28),  $\bar{F}$  is a nondimensional parameter for the tip load,  $\bar{Q}$  is a nondimensional stiffness parameter, and  $Q_{cr}$  is the critical Euler buckling load for a uniform cantilevered beam for which  $I(x)=I_1$ . In this linear elastic perfectly-plastic case,  $\bar{y} = \bar{y}_{la}$ ,  $\bar{y}_p = \bar{y}_{la}$  at  $\bar{x} = \bar{x}_p$ , and  $\bar{y}_2 = \bar{y}_{la}$  at  $\bar{x} = 1$ . For this case,  $F_{GP}$  is still higher than the true static plastic collapse load since the effects of the change of beam geometry and the spread of the plastic zone during loading are not included. However,  $F_{GP}$  of this linear elastic perfectly plastic case is lower than that of the rigid perfectly plastic case.

## 5. Numerical results and discussion

In this section, numerical results are presented for the five beam models in which the respective plastic collapse loads  $F_{GP}$  and their locations  $x_p$  are compared. The definitions and short designations for the three basic beam models analyzed herein are: rigid perfectly plastic (RP); elastic perfectly plastic (EP) without consideration of geometric changes during elastic loading; and elastic perfectly plastic with geometric changes accounted for during elastic loading (EPG). For comparison purposes, numerical results are also included for two other models: a discrete frame model (EPFRAME), and a finite element model (FE), both commercially available computer programs capable of elastic perfectly plastic analysis. Numerical results for all five beam models are based on the following reference parameter:  $L_b = 1.0$  m,  $d_b = 0.1$  m,  $E = 200$  GN/m<sup>2</sup>,  $\sigma_y = 345$  MN/m<sup>2</sup>,  $t = 0.003$  m,  $s_1 = 0.2$  m,  $\alpha_1 = 0.96$ ,  $s_2 = 0.185$  m,  $\alpha_2 = 0.35$ ,  $\eta_1 = 0.059$ ,  $\eta_2 = 0.094$ ,  $\eta_3 = 0.313$ ,  $\eta_4 = 0.254$ , and  $\eta_5 = 0.092$ .

For the chosen reference parameters, it was determined that certain simplifying assumptions could be made to efficiently compute the desired results for the first three beam models, RP, EP, and EPG. First, the locations of the two neutral bending axes (Fig. 2), CPA for elastic action and EAA for fully plastic action, differed at most by 1% along the beam length; and the exact value of  $I(x)$  given by Eq. (2d) differed at most by 4% from the approximate  $I_a(x)$  of Eq. (25), where the mean difference along the length was about 2%. Second, when the exact linear deflection curve,  $\delta y_l(x) = y_l(x) - y_o(x)$ , where  $y_l(x)$  was computed numerically using *Mathematica*, was compared to the approximate deflection curve  $\delta y_{la}(x)$ , where  $y_{la}(x)$  was computed using Eq. (28), the results were

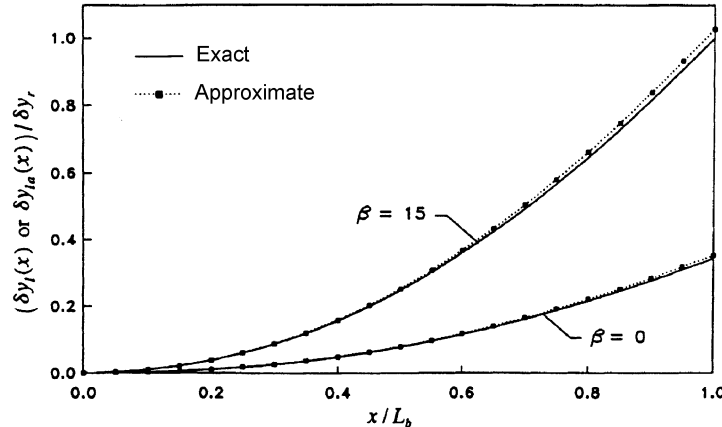


Fig. 3 Linear elastic deflection curves for  $b=0$  and 15 degrees, in which Exact denotes the results using MATHEMATICA and Approximate denotes the results using Eq. (28)

nearly the same. See Fig. 3. These curves, normalized with respect to  $\delta y_r = \delta y_i(L_b)$  for  $\beta=15$  degrees, show that the maximum error between the exact and approximate tip deflection is at most 3%. Such results justify the use of two simplifying assumptions in the calculations for the first three beam models: coincidence of the axes CPA and EAA, and the use of Eq. (25) for calculating  $I_a(x)$ . These simplifying assumptions were not used, however, for the last two discrete beam models.

Consider the first two beam models: the one of a rigid perfectly plastic (RP) material and the other of a linear elastic perfectly plastic (EP) material. Using Eqs. (14) and (15), the effect of  $\beta$  on the gross plastic collapse load  $F_{GP}$  and the corresponding location of the plastic hinge  $x_p$  were computed and are shown in Figs. 4(a) and 4(b), respectively. Included in Figs. 4 are also the results for the fourth beam model: an elastic perfectly plastic model based on EPFRAME, a computer program for elastic perfectly plastic plane frame analysis (Lee and Goel 1986). For this latter program, the tapered beam was discretized to 100 uniform beam elements, where the fully plastic moment of each element, without normal compressive loads ( $k_1=0$ ), was calculated at the mid-length of the element. The numerical results shown in Figs. 4 are summarized. First,  $F_{GP}$  and  $x_p$  for the RP model ( $k_1=0$ ), are in very good agreement with those of EPFRAME. The small differences,

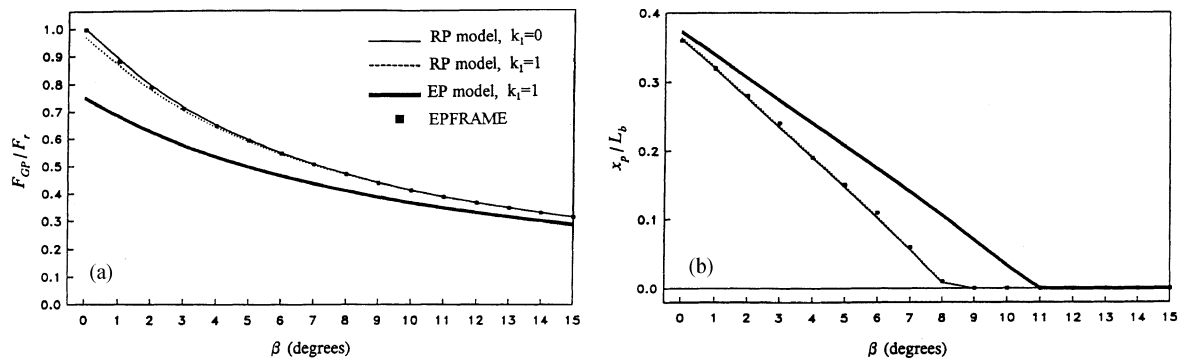


Fig. 4 Comparison of several beam models showing the effect of  $b$  on: (a) plastic collapse load; (b) plastic hinge location

especially for  $x_p$ , are probably due to the discretization of the beam model. Second, in Fig. 4(a) in which the load is normalized with respect to  $F_r = F_{GP}$  of the RP model ( $k_1=0$  and  $\beta=0$ ),  $F_{GP}$  decreases monotonically as  $\beta$  increases. Also, the influence of the normal compressive force on  $F_{GP}$  for the RP model is small and decreases as  $\beta$  increases.  $F_{GP}$  for the EP model is less than for the RP model, where this difference decreases from about 30% for  $\beta=0$  to less than 10% for  $\beta=15$  degrees. Third, it is observed in Fig. 4(b) that the relation between  $\beta$  and  $x_p$  is almost linear for the RP model as well as for the EP model. As the load angle increases  $x_p$ , moves toward the fixed end. Also,  $x_p$  for the RP model approaches the fixed end at a smaller  $\beta$  compared to that for the EP model. In the calculations for Figs. 4, the crush load ratio at the plastic hinge was  $\lambda(x_p) \leq (1-4\eta_2)=62.4\%$ , which justifies the use of Eqs. (14) and (15) in which the effect of the shear force on  $F_{GP}$  was ignored.

Shown in Figs. 5(a) and 5(b), respectively, are the effects of the initial beam's tip displacement on the plastic collapse load and on the location of the plastic hinge, for  $\beta$  values in the range of 0 to 15 degrees, all based on the EP beam model. Note that for the high range of  $\beta$ , the contribution of the transverse force component of the tip load to  $M(x)$  is larger than that of the longitudinal force component and the effect of  $d_b$  is therefore reduced. Note that in Fig. 5(b), except for  $\beta=0$ ,  $x_p$  moves away from the fixed end as  $d_b$  increases. However,  $x_p$  is slightly affected by  $d_b$  for small  $\beta$ -angles.

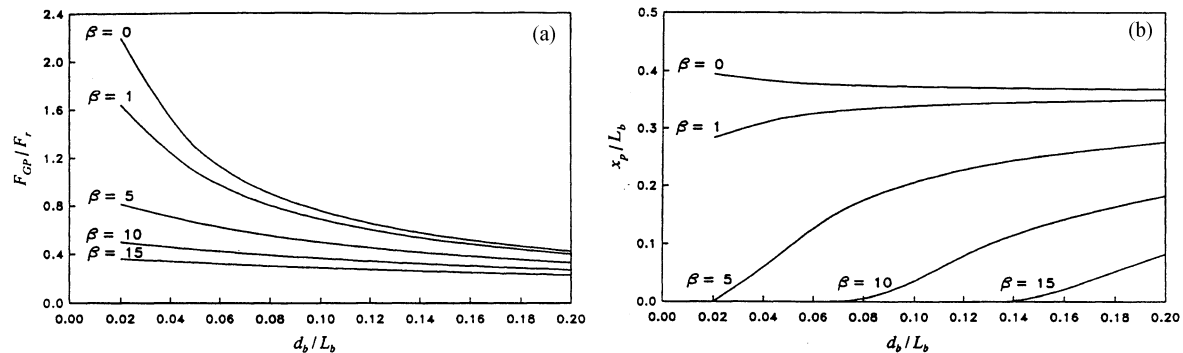


Fig. 5 Results for the elastic perfectly plastic (EP) beam model showing the effect of initial tip displacement on: (a) plastic collapse load; (b) plastic hinge location

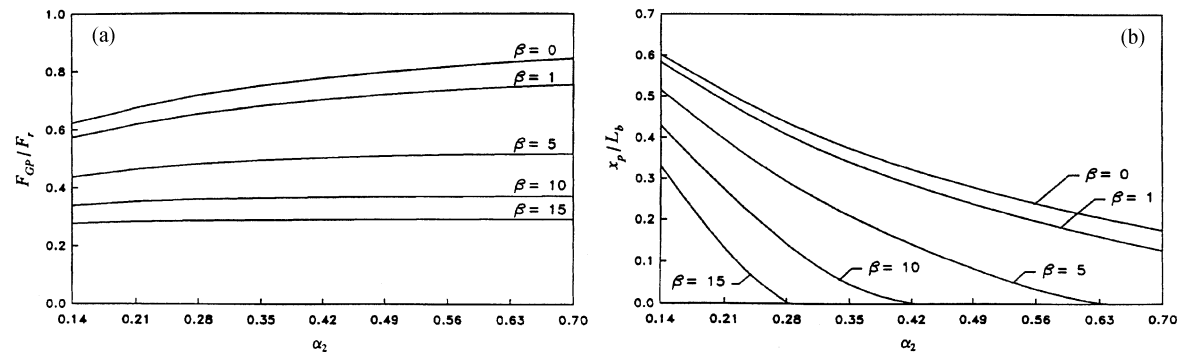


Fig. 6 Results for the elastic perfectly plastic (EP) beam model showing the effect of angle of corrugation on: (a) plastic collapse load; (b) plastic hinge location

For moderate and large  $\beta$ -angles, the plastic hinge occurs away from the fixed end ( $x_p > 0$ ) if  $d_b$  exceeds a critical value. This critical value is, for example, 2% of  $L_b$  for  $\beta = 5$  degrees and 14% of  $L_b$  for  $\beta = 15$  degrees. As  $d_b$  increases beyond the critical value, the effect of  $d_b$  on  $x_p$  is initially significant and then decreases.

Shown in Figs. 6(a) and 6(b), respectively, are the effects of the tip corrugation angle  $\alpha_2$  on  $F_{GP}$  and on  $x_p$ , both for the EP beam model ( $k_1 = 1$ ) and for five values of  $\beta$ . As expected,  $F_{GP}$  decreases as  $\alpha_2$  decreases since the fully plastic moment of the W-section of the beam decreases, Fig. 6(a). For very small  $\beta$ -angles, the decrease in  $F_{GP}$  is larger than that for moderate and large  $\beta$ -angles. For  $\beta = 0$ , the decrease in  $F_{GP}$  for  $\alpha_2 = 0.14$  is about 27% when compared to  $\alpha_2 = 0.70$ , while this decrease is only about 6% for  $\beta = 15$  degrees. For  $\alpha_2 = 0.14$  the taper ratio  $\kappa$  is 0.023 and the difference between the exact and approximate second area moment is at most 7%; but these values for  $\alpha_2 = 0.70$  are 0.482% and 0.5%, respectively. Thus, for small taper ratios of less than 0.1, the assumption of small elastic deformations may not be adequate as the beam undergoes relatively large elastic deformations. It is noted that  $x_p$  moves away from the fixed end as  $\alpha_2$  decreases, Fig. 6(b). The plastic hinge occurs away from the fixed end ( $x_p > 0$ ) if  $\alpha_2$  is less than a critical value. For example, this critical value is 0.63 for  $\beta = 5$  degrees and 0.28 for  $\beta = 15$  degrees. As  $\alpha_2$  decreases below the critical value, the effect of  $\alpha_2$  on  $x_p$  is initially small and then increases significantly, especially for large  $\beta$ -angles.

Consider now the third beam model RPG, the elastic perfectly plastic model in which the change of beam geometry during elastic loading is incorporated so that this effect on the plastic collapse load  $F_{GP}$  may be discerned. Define this collapse load as that at the point of intersection of the elastic buckling curve and the rigid perfectly plastic mechanism curve of a beam-column. To determine this point of intersection, the first step was to compute the elastic buckling curve,  $F_b$  vs.  $y_{2b}$ . This curve was derived by solving the governing differential equation (Wilson and Strong 1997), using the stated reference parameters,  $I_a(x)$  of Eq. (25), and the numerical methods of *Mathematica*. Second, the rigid perfectly-plastic mechanism curve was derived based on the mechanism shown in Fig. 7. For small plastic hinge rotations,  $M_{FP}(x)$  at the plastic hinge and  $\beta$  were assumed to be constant and  $N(x)$  was ignored. It follows that the rigid perfectly-plastic mechanism curve,  $F_m$  vs.  $y_{2m}$ , can be expressed as

$$F_m = \frac{M_{FP}(x_p)}{(y_{2m} - y_o(x_p)) \cos \beta + \sin \beta \sqrt{(L_b - x_p)^2 + (d_b - y_o(x_p))^2 - (y_{2m} - y_o(x_p))^2}} \quad (32)$$

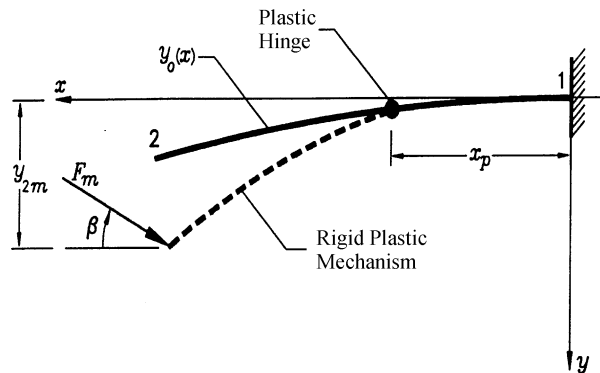


Fig. 7 Rigid perfectly plastic mechanism of the initially curved, cantilevered beam

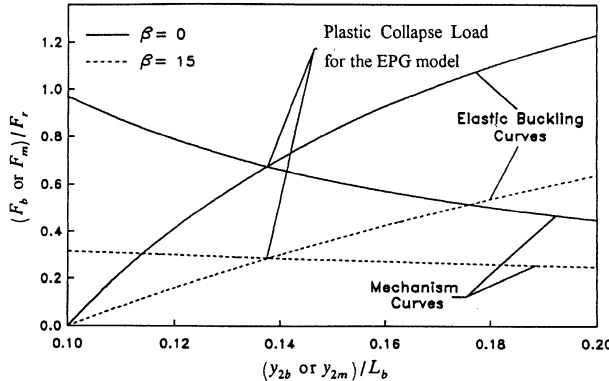


Fig. 8 Elastic buckling and rigid perfectly plastic mechanism curves for  $b=0$  and 15 degrees

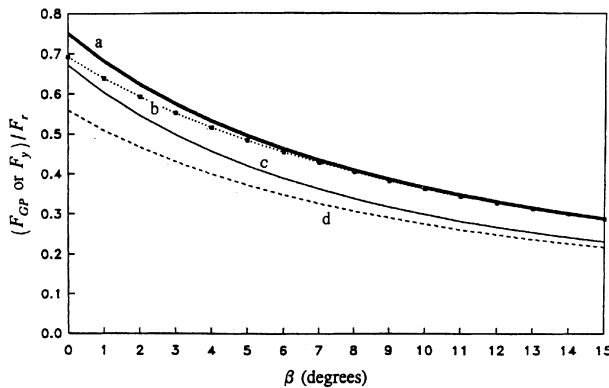


Fig. 9 Comparison of plastic collapse loads and loads for first yield for several beam models: (a) for the EP beam; (b) for the EPG beam; (c)  $F_y$  for the RP beam; (d)  $F_y$  for the EP beam

where  $M_{FP}(x)$  is given by Eq. (5b) and  $y_o(x)$  is given by Eq. (1). The results of these calculations for  $\beta=0$  and 15 degrees are shown in Fig. 8. The point of intersection of these two curves  $F_{GP}$  is for the EPG model, a value that is somewhat higher than the “true” plastic collapse load because the spread of the plastic zone along the beam was ignored in the model. The elastic buckling curves of Fig. 8 approach asymptotically the expected elastic buckling loads. For both values of  $\beta$ , the elastic buckling loads are higher than  $F_{GP}$  of the EPG model, which indicates that the beam fails plastically.

Shown in the top two curves of Fig. 9, as a function of  $\beta$ , are comparisons of the plastic collapse loads  $F_{GP}$  for the second (EP) and third (EPG) beam models. These results show that the effect of the change of beam geometry during loading on  $F_{GP}$  is relatively high for small  $\beta$ -angles (an 8% difference for  $\beta=0$ ); but is small for moderate  $\beta$ -angles (less than 3% for  $\beta=5$  degrees and less than 0.5% for  $\beta=15$  degrees). Shown in the lower two curves of Fig. 9 are comparisons of the loads at first yield at the plastic hinges, or  $F_y$ , for the first (RP) and second (EP) beam models. These latter two yield loads were calculated using classical beam theory in which the compressive normal force was included. The difference between  $F_{GP}$  of the EP model and  $F_y$  of the RP model is at most 11% for  $\beta=0$ , while that difference is higher, but at most 20% for  $\beta=15$  degrees.

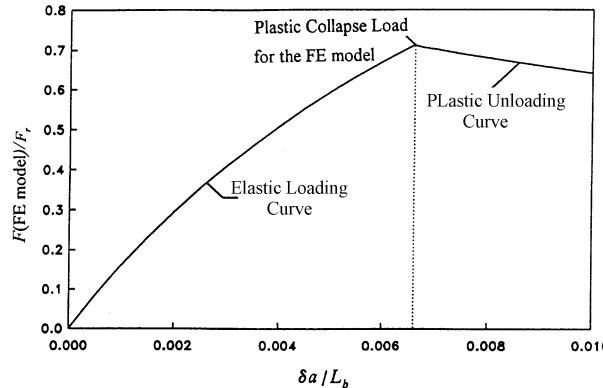


Fig. 10 Tip load-tip displacement behavior based on the finite element (FE) beam model and  $\beta=0$

The gross plastic collapse loads of the third beam model (EPG) were also compared to those computed using a fifth beam model based on finite elements (FE). For the latter studies, the NIKE3D code was used (Maker *et al.* 1991), in which an elastic perfectly plastic material was assumed and geometry changes during loading were included. For each beam element, 100 in all, each midlength had a rectangular cross-sectional area  $A(x)$  and a second area moment  $I(x)$  equal, respectively, to that based on the reference parameters. The plastic collapse load was computed by first applying an incremental tip displacement  $\delta a$  in the desired direction of the tip load, or the quasi-static displacement control method. Then, the tip load-displacement history corresponding to  $\delta a$  was computed. A typical tip load-displacement history obtained from this finite element model is shown in Fig. 10 for the case of  $\beta=0$ . It is observed that, as  $\delta a$  is increased, the corresponding tip load  $F$  increased during elastic loading, peaked, and then decreased during plastic unloading. The point of intersection of the elastic loading curve and the plastic unloading curve (the peak) is the plastic collapse load. The transition from the elastic loading curve to the plastic unloading curve occurred suddenly since the finite element beam model is a skeletal representation in which the spread of the plastic zone is neglected. Here,  $F_{GP}$  of the FE model is still higher than the “true” plastic collapse load. Summarized in Table 1, for several angles  $\beta$ , are values of  $F_{GP}$  for the EPG model, normalized with respect to  $F_{GP}$  of the FE model. These results show that  $F_{GP}$  of the EPG

Table 1  $F_{GP}$  for the EPG beam model, normalized with respect to  $F_{GP}$  of the FE beam model

$\beta$ (degrees)	0	2	4	6	8	10	12	15
$\frac{F_{GP}(\text{EPG model})}{F_{GP}(\text{FE model})}$	0.97	0.97	0.97	0.96	0.96	0.94	0.93	0.93

Table 2 Mechanical properties of the experimental specimens

	Test 1	Test 2
Young's modulus (GPa)	200.	210.
Yield stress (MPa)	285.	287.
Ultimate stress (MPa)	379.	380.
Initial stress coat cracking (MPa)	313.	335.

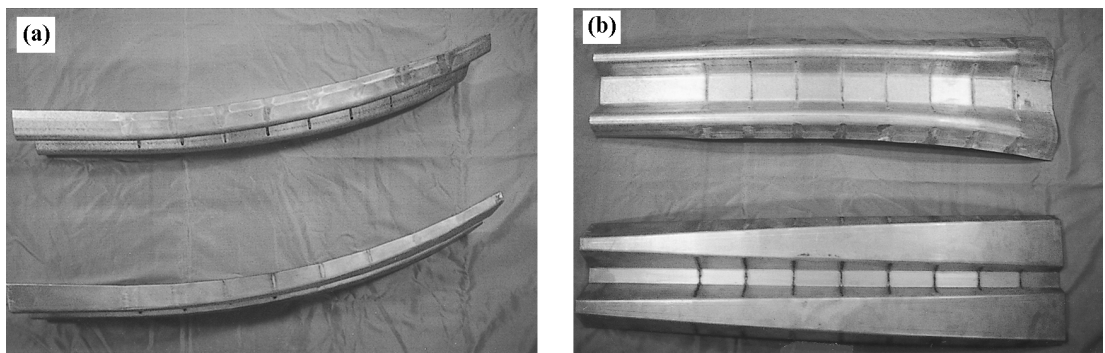


Fig. 11 Laboratory-scale models, types I and II: (a) plan views; and (b) side views (The unclamped length is 63.5 cm, the flare opens from left to right, and the tip is at the right)

model and  $F_{GP}$  of the FE model differ from 3% to 7%.

## 6. The experiments

Experiments using two types of tapered, initially curved, and transversely corrugated cantilevered beams were designed and implemented to measure both static plastic collapse loads and low speed impact collapse loads, together with the collapse locations along the beams. These test specimens were designed as half-scale versions of practical highway guardrail terminals and their detailed engineering drawings are available in the report of Wilson and El-Esnawy (1997). Shown in Fig. 11(a) and 11(b) are photographs of these specimens: type I with rounded tops and type II with flat tops on the outside corrugations. For both configurations, the unclamped length was 63.5 cm, the wall thickness was 1.83 mm (14 gage steel); and both had the same taper (side view), and the same initial curvature (plan view).

In preliminary experiments, the tensile properties of the steel sheet used for the cantilevered specimens were measured using tensile specimens designed according to ASTM standards. These specimens, as well as the cantilevered beam specimens, were precoated with Stress Coat, a paint that produced small visible cracks as the beam yielded. The results of two tensile tests are shown in Table 2. The three mechanical properties, Young's modulus, yield stress, and ultimate stress, as well as the initial stress at which cracking of the Stress Coat became visible, were quite consistent between the two specimens. The flow stress for plastic collapse of the cantilevered beam specimens was then defined as the mean value of the yield stress and the ultimate stress measured in these tensile experiments, or 333 MPa.

For economical reasons, the two types of beam specimens used in both the static and impact experiments were not die-stamped, as they would be for mass production. Instead, the corrugations were first formed in a mechanical "break" as a straight, uniform section, starting with a flat, rectangular sheet. Next, using a mechanical press, the corrugations were flared by nonuniform flattening along the length, in which the corrugations were filled with polyurethane strips so that corrugation buckling was avoided during pressing. The initial curvature was then achieved by first sawing transverse cuts every seven centimeters apart, about half way through the height of each corrugation; and then by bending the specimen, nearly closing the gaps to the desired curvature. The cuts were then carefully filled with a low temperature steel-bronze weld that had approximately

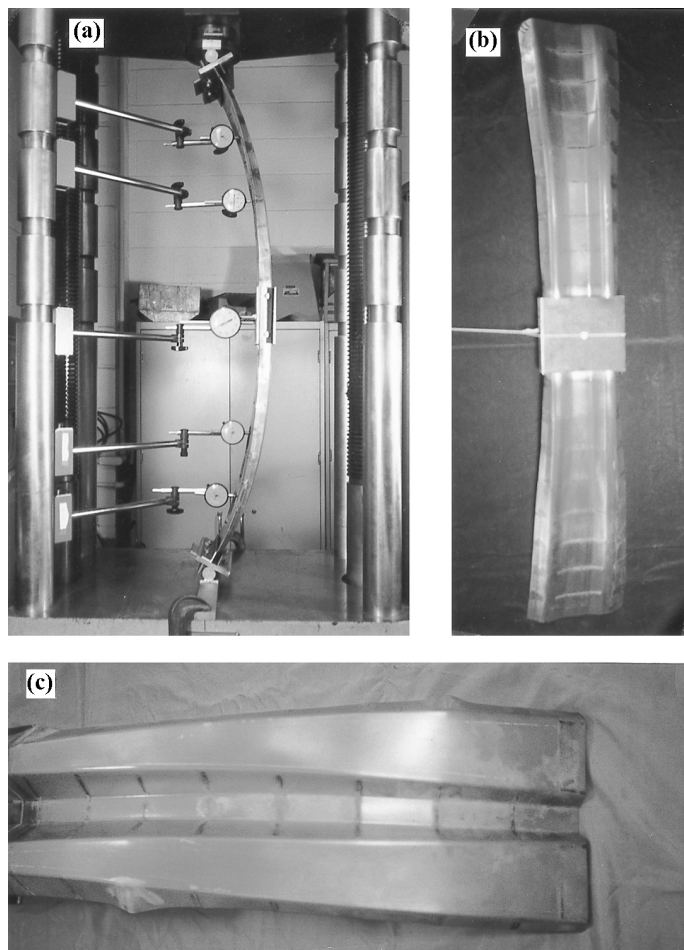


Fig. 12 Views of the double static specimen: (a) edge view as mounted in the testing machine; (b) side view; and (c) side view showing static buckling

Table 3 Static collapse characteristics of the experimental models

		Specimen type I (rounded-top)	Specimen type II (flat-top)
Elastic buckling load (kN)	Analysis	—	9.43
Plastic collapse load (kN)	Analysis	9.61	7.08
	Experiment	2.89	4.45
Location from fixed end for plastic collapse (inches)	Analysis	25.4	26.2
	Experiment	25.7	18.0

the same yield strength as that of the steel beam, and the welds were polished smooth with the specimen face. The welded cuts on the final models are seen in the photographs of Figs. 11.

Photographs for a typical static experiment with a double specimen mounted in a universal testing machine, and also standing alone, are shown in the photographs of Figs. 12(a) and 12(b). This

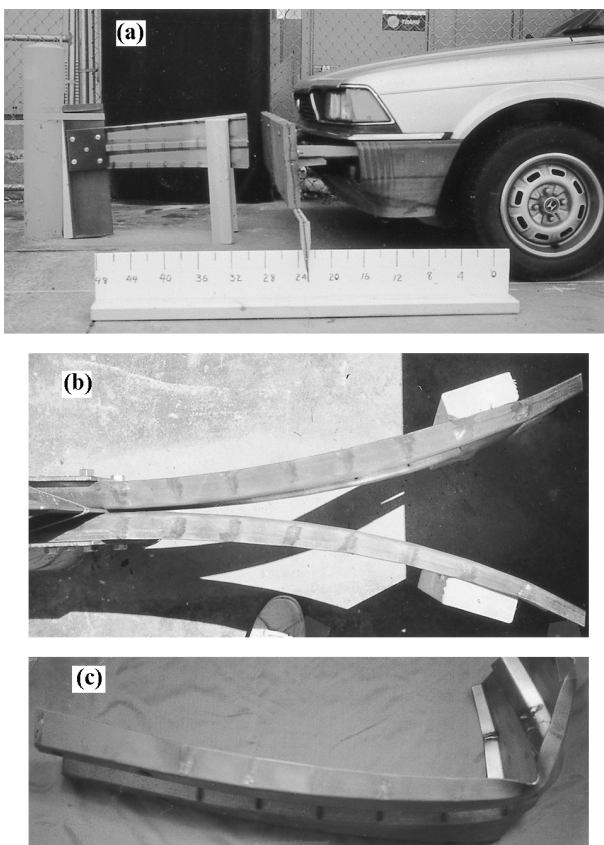


Fig. 13 Impact experiments showing: (a) setup and test car; (b) plan view of the Y- specimen configuration; and (c) plastic collapse from impact of a type-II specimen

double specimen configuration consists of two identical single specimens securely bolted together at their fixed ends. The midlength of the double specimen simulated the fixed end. Since the extreme ends were on roller supports, each specimen behaved as fixed-free beam when the end loads were applied by the universal testing machine.

Observations of the static behavior of specimen types I and II are summarized in Table 3. For type I and II specimens, the computed elastic buckling was nearly the same, 9.43 kN. In the experiments, however, elastic buckling did not occur. Gross plastic collapse occurred at loads lower than 9.43 kN, or at 2.89 kN for type I and 4.45 kN for type II specimens. The main reason that the gross plastic collapse load was only about one-third of the predicted value for type I was that premature buckling occurred at the lower roller support. This was avoided in later tests for type II specimens by adding polyurethane inserts at the roller supports, under the corrugations. Thus, type II specimens collapsed at the higher load of 4.45 kN, which was closer to the predicted value of about 7.08 kN. There are two main reasons for this latter difference: (1) the actual spread of the plastic zone as collapse was approached, observed by the progressive cracking of the Brittle Coat during the experiments, was not accounted for in the analysis; and (2) large changes in geometry during the approach to plastic collapse were also not included in the elastic perfectly plastic analysis. The analysis gave an upper bound for the collapse load. The last important observation

was that plastic collapse occurred away from the fixed end, at the 40% and the 28% points (25.7 cm and 18.0 cm, respectively), whereas the analysis predicted that plastic collapse would occur at about the 40% points (25.4 cm and 26.2 cm), for types I and II specimens, respectively. A photograph of plastic buckling for a type II specimen, which was similar in character to that of type I specimen, is shown at the bottom of Fig. 12.

The experimental setup for the dynamic impact experiments is shown in the Fig. 13(a); and a closeup plan view of a like pair of test specimens, a Y-configuration, is shown in Fig. 13(b). The test car of 1110 kg mass when fully loaded, was fitted with a steel plate over a wood plank that replaced the front bumper for specimen impact. The test car freely rolled down an incline and its speed just prior to impact was tracked with a video camera that recorded at every 1/30th of a second the location of the pointer on the bumper along the distance scale on the road. See Fig. 13(a). The car's shock absorbers were blocked so that they were not operational. An accelerometer attached to the cars chassis at the mass center, was coupled to an onboard signal conditioner and recorder, and was used to measure the cars deceleration during impact with specimens. The like pair of the Y-configured beam specimens were bolted back-to-back to the flange of a T-beam, which in turn was banded to a fixed steel post that served as the backup constraint. The wood breakaway post near the front flare of each specimen of this Y-configuration helped to hold the configuration in place before impact, but contributed nothing to the specimen's bending stiffness. During impact, which was always somewhat eccentric (each of the Y-pair was never impacted simultaneously), only one of the two buckled plastically, the one that was impacted first. Just after impact, the Y-assembly then rotated somewhat around the backup post. An example of plastic collapse for a type II impacted specimen is shown in Fig. 13(c).

The results for the dynamic impact experiments are summarized in Table 4. These results are for test car speeds just prior to impact of 8.1 km/h; for measured peak impact decelerations for the respective specimen types I and II of 3.1g and 2.6g; and for impact durations of about 0.1 s. The first set of results are the respective plastic collapse loads for specimens I and II: 33.8 kN and 28.3 kN. For type II specimen, the *mean* load over the impact time was about 4.4 kN, which was close to the static plastic collapse load of 4.45 kN reported in Table 3. It is noted that type I specimens are stronger than type II specimens, which would be expected since the curved top corrugations of type I specimens offer a higher transverse bending stiffness than the flat top corrugations of type II specimens. The second set of results are that there are three points of plastic collapse along each specimen, varying from about 39 cm to about 45 cm from the fixed end, depending whether the collapse is at the top edge, at the center, or at the bottom edge on the transverse section. Thus, since the unconstrained lengths if the test specimens were 63.5 cm, plastic collapse occurred between 61% and 71% of the specimens length from the fixed end. These results are in contrast to those for static plastic collapse where the counterpart locations were at the 40% and the 28% points, much closer to the fixed end.

Table 4 Measured dynamic characteristics of the experimental models

	Type I (rounded-top)	Type II (flat-top)
Peak load for plastic collapse (kN)	33.8	28.3
Location of plastic collapse modes: at top; at center; at bottom edge (cm)	39.1; 43.9; 40.1	40.6; 44.5; 40.1

The experimental results on half-scale specimens may be scaled to those for full-scale or prototype size, provided that the designs remain geometrically similar, or nearly so. For scaling purposes, the dimensionless system parameters defined by Eqs. (16)-(20) should remain invariant, and all of these except Eq. (18) are automatically invariant if geometric similarity is maintained. For example, for a prototype geometrically similar to model type I, the point or region of plastic collapse will occur at about 40% the overall length from the fixed end. Eq. (18), which defines the nondimensional plastic collapse load, must also remain invariant, and this equation may be used to compute the plastic collapse load for the prototype whose material is the same but whose size, thickness, and yield stress may be different from the model. For example, suppose the half-scale width factor  $s$  (and therefore the overall geometry except thickness  $t$ ) increases by a factor of two, the thickness  $t$  increases by a factor of 1.5, and the yield strength remains the same from the model to the prototype. Then for specimen type II, Table 3, the plastic collapse load would increase from 4.45 kN to  $(2)(1.5)(4.45)=13.35$  kN for the prototype. It is further hypothesized that the peak dynamic or impact load would also increase by this same factor of three, from 28.3 kN measured for the type II model, to 84.9 kN for the full-scale prototype. This last calculation does need further verification through dynamic analysis and full-scale testing.

## **7. Conclusions**

Numerical parametric studies that employed several static plastic collapse theories for tip-loaded, tapered, and initially curved cantilevered beams of corrugated cross sections, lead to some common conclusions. First, for shallow angles of the tip load, the location of the plastic hinge (the location of the plastic collapse load) from the fixed end was especially sensitive to the type of tapering (outward from the fixed end); but the magnitude of the collapse load was less sensitive to such tapering. Second, as the corrugation angle at the loaded end was decreased, the plastic hinge moved away from the fixed end and the plastic collapse load was reduced. Third, as the initial transverse tip displacement was increased beyond a critical value, the plastic hinge moved away from the fixed end, an effect that was more pronounced for increasing angles of the tip load; however, an increase in this initial tip displacement always effected a significant decrease in the plastic collapse load.

These general conclusions were found to be valid regardless of the static model used in the calculations. The numerical results showed only small differences in the plastic collapse loads and their locations when the results of the following five models were compared: closed form solutions based on rigid perfectly plastic theory (RP); solutions based on elastic perfectly plastic theory, without (EP) and with (EPG) the incorporation of large elastic geometric changes during loading; and two packaged computer programs: an elastic perfectly plastic beam frame model (EPFRAME) and an elastic perfectly plastic finite element (FE) model. Those differences are summarized. First, for tip loading angles up to 15 degrees, the plastic collapse loads for the RP model were within 10% to 20% of those loads computed from the EP and EPG models. Second, the plastic collapse loads differed by less than 10% when the results computed from the intersection of the elastic buckling and RP mechanism curves were compared to the results obtained using the EP model with linear elasticity. These load differences decreased, however, as the angle of the tip load approached zero. Third, the plastic collapse loads based on the EPG model were within 10% of those predicted by the EPFRAME program and by the FE program, for which the latter included the large elastic geometric changes during loading.

The experimental results, both static and low velocity impact, complemented the results of theory. These experiments were performed on beam models that were half-scale geometrically compared to those considered applicable to future highway guardrail terminals. These results are summarized. First, all of the five theoretical models investigated herein gave a reasonable upper bound for the static plastic collapse load. Second, the location of the computed static plastic collapse point was at 40% of the beams length from the fixed end, which complemented the measured values of 40% and 28% in two different specimens. Third, the low velocity impact experiments showed that the points of plastic collapse moved from the statically predicted 40% point from the fixed end to between the 61% and 71% points. Fourth, the mean impact loads for plastic collapse were about the same for the static and dynamic experiments; but the peak dynamic loads at plastic collapse exceeded those of the static cases by about a factor of six. Fifth, similitude rules based on static theory, together with the results of impact experiments and necessary further developments of the dynamic theory, will greatly advance prototype designs of properly tapered, initially curved, corrugated beams for safer, non-vehicle penetrating guardrail terminals for the world's highways.

## Acknowledgements

This research was supported in part by the National Academy of Sciences under contract NCHRP-34 to Duke University. The finite element code NIKE3D was supplied by Lawrence Livermore National Laboratory under the Methods Development Group Collaborators Program.

## References

- Al-Gahtani, H.J. (1996), "Exact stiffnesses for tapered members", *Journal of Structural Engineering*, **122**(10), 1234-1239.
- Dinnik, A. (1932), "Design of columns of varying cross-section", *Transactions of Applied Mechanics*, **54**(APM-54-16), 165-171.
- El-Esnawy, N.A. (1997), "Analysis and design of tandem vehicles and guardrail breakaway cable terminals for safer highways", Ph.D. Dissertation, Department of Civil and Environmental Engineering, Duke University, Durham, North Carolina.
- Ermopoulos, J.C. (1986), "Buckling of tapered bars under stepped axial loads", *Journal of Structural Engineering*, **112**(6), 1346-1354.
- Horne, M.R. (1979), *Plastic Theory of Structures*, 2nd ed., Pergamon Press, New York.
- Horne, M.R. and Morris, L.J. (1982) *Plastic Design of Low-Rise Frames*, MIT Press, Cambridge, Massachusetts.
- Karabalis, D.L. and Besko, D.E. (1983), "Static, dynamic, and stability analysis of structures composed of tapered beams", *Computers and Structures*, **16**(6), 731-748.
- Lee, H. and Goel, S. (1986), "Program EPFRAME: Elastic-plastic analysis of plane frames", Department of Civil and Environmental Engineering, University of Michigan, Ann Arbor, MI (unpublished).
- Maker, B.N., Ferencz, R.M. and Hallquist, J.O. (1991), *NIKE3D: A Nonlinear, Implicit, Three-Dimensional Finite Element Code for Solid and Structural Mechanics-User's Manual*, University of California, Lawrence Livermore National Laboratory, Rept. UCRL-MA-105268.
- Pigman, J.G. and Agent, K.R. (1988), "Performance evaluation of breakaway-cable-terminal end treatments", *Transportation Research Record* 1198, TRB, National Research Council, 1-10.
- Siginer, A. (1992), "Buckling of columns of variable flexural rigidity", *Journal of Engineering Mechanics*, **118**(3), 640-643.
- Timoshenko, S.P. and Gere, J.M. (1961), *Theory of Elastic Stability*, McGraw-Hill Book Company, Inc., New

- York.
- Williams, F.W. and Aston, G. (1989), "Exact or lower bound tapered column buckling loads", *Journal of Structural Engineering*, **115**(5), 1088-1100.
- Wilson, J.F. and El-Esnawy, N.A. (1997), "The highway guardrail infrastructure: safer terminal design", Final Report, Contract No. NCHRP-34, Transportation Research Board, National Academy of Sciences, 1-32.
- Wilson, J.F. and Strong, D.J. (1997), "Elastic buckling of end-loaded tapered cantilevered beams with initial curvature", *Structural Engineering and Mechanics*, **5**(3), 257-268.
- Wolfram, S. (1993), *Mathematica. A System for Doing Mathematics by Computer*, 2nd ed., Addison-Wesley Publishing Company, Inc., New York.

## Appendix

$$G_1(\alpha_x) = 2\eta_2 \frac{(1 - \cos \alpha_x)}{\alpha_x} + \eta_3 \sin \alpha_x \quad (A1)$$

$$\begin{aligned} G_2(\alpha_x) = & \frac{[(\eta_3 - 2\eta_4)\eta_5 + 2(\eta_3 - \eta_4)\eta_4]}{4} \sin \alpha_x + \eta_2^2 \frac{(\sin \alpha_x + \alpha_x)}{\alpha_x^2} \\ & + \frac{(8\eta_2 + 2\eta_3 + 2\eta_4 + \eta_5)}{4} + G_1(\alpha_x) \end{aligned} \quad (A2)$$

$$G_3(\alpha_x) = (6\eta_3 + 6\eta_4 + 1.5\eta_5 + 48\eta_2)G_1^2(\alpha_x) + 96\eta_2^2 \frac{(\sin \alpha_x - \alpha_x)}{\alpha_x^2} G_1(\alpha_x) \quad (A3)$$

$$+ [12(\eta_3 - \eta_4)\eta_4 + 3(\eta_3 - 2\eta_4)\eta_5] \sin \alpha_x G_1(\alpha_x)$$

$$+ [2(\eta_3^3 + \eta_4^3) + 6(\eta_3 - \eta_4)^2 \eta_4 + 1.5(\eta_3 - 2\eta_4)^2 \eta_5] \sin^2 \alpha_x$$

$$+ 36\eta_2^3 \frac{[\alpha_x^2 + 0.5\alpha_x \sin(2\alpha_x) - 2\sin^2 \alpha_x + 2(\sin \alpha_x - \alpha_x)^2]}{\alpha_x^4} + 2\eta_5^3 \sin^2 \gamma(x) - 24G_2^2(\alpha_x)$$

$$G_4(\alpha_x) = \eta_2 \left( \frac{(1 - \cos \alpha_x)}{\alpha_x} + \frac{(4\eta_2 + 4\eta_3 - 1)}{4} \sin \alpha_x \right) \quad (A4)$$

$$\begin{aligned} G_5(\alpha_x) = & \frac{[(4\eta_2 + 4\eta_3 - 1)^2 + 2(1 - 4\eta_2)^2 + (4\eta_2 + 4\eta_4 - 1)^2 + 4(2\eta_4 - \eta_3)\eta_5]}{32} \sin \alpha_x \\ & + (2\eta_2 - 0.25\eta_5)G_1(\alpha_x) + (1 - 4\eta_2 - \eta_3 - \eta_4)G_4(\alpha_x) + 3\eta_2^2 \frac{(\sin \alpha_x - \alpha_x)}{\alpha_x^2} \end{aligned} \quad (A5)$$